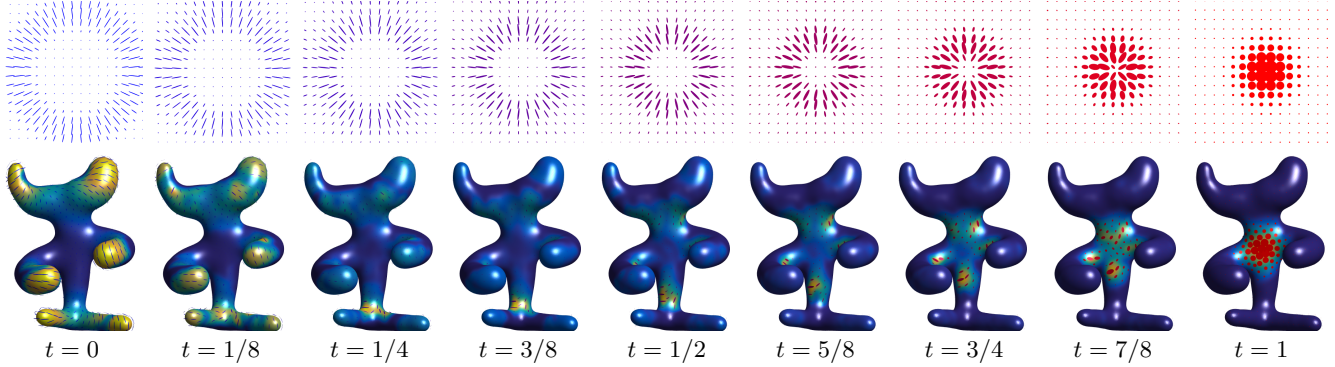


# Quantum Optimal Transport for Tensor Field Processing



**Figure 1:** Given two input fields of positive semidefinite matrices (displayed at times  $t \in \{0, 1\}$  using ellipses) on some domain (here, a 2-D planar square and a surface mesh), our Quantum Optimal Transport (Q-OT) method defines a continuous interpolating path for  $t \in [0, 1]$ . Unlike linear interpolation schemes, Q-OT transports the “mass” of the tensors (size of the ellipses) as well as their anisotropy and orientation. This interpolation, and its extension to finding the barycenter of several input fields, is computed using a fast extension of the well-known Sinkhorn algorithm.

## 1 Abstract

This article introduces a new notion of optimal transport (OT) between tensor fields, which are measures whose values are positive semidefinite (PSD) matrices. This “quantum” formulation of OT (Q-OT) corresponds to a relaxed version of the classical Kantorovich transport problem, where the fidelity between the input PSD-valued measures is captured using the geometry of the Von-Neumann quantum entropy. We propose a quantum-entropic regularization of the resulting convex optimization problem, which can be solved efficiently using an iterative scaling algorithm. This method is a generalization of the celebrated Sinkhorn algorithm to the quantum setting of PSD matrices. We extend this formulation and the quantum Sinkhorn algorithm to compute barycenters within a collection of input tensor fields. We illustrate the usefulness of the proposed approach on applications to procedural noise generation, anisotropic meshing, diffusion tensor imaging and spectral texture synthesis.

**Keywords:** Optimal transport, tensor field, PSD matrices, quantum entropy

**Concepts:** •Computing methodologies → Shape analysis;

## 1 Introduction

Optimal transport (OT) is an active field of research at the intersection of probability theory, PDEs, convex optimization and numerical analysis. OT offers a canonical way to lift a ground distance on some metric space to a metric between arbitrary probability measures defined over this base space. OT distances offer many interesting features, and in particular lead to a geometrically faithful way to manipulate and interpolate probability distributions.

Permission to make digital or hard copies of part or all of this work for personal or classroom use is granted without fee provided that copies are not made or distributed for profit or commercial advantage and that copies bear this notice and the full citation on the first page. Copyrights for third-party components of this work must be honored. For all other uses, contact the owner/author(s). © 2017 Copyright held by the owner/author(s).

### 28 1.1 Previous Work

**29 Scalar-valued optimal transport.** Dating back to the eighteenth century, classical instances of the optimal transport problem seek 30 a minimal-cost matching between two distributions defined over 31 a geometric domain, e.g. matching supply to demand while incurring 32 minimal cost. Initially formulated by Monge in terms of an 33 unknown map transporting mass [1781], its reformulation by Kan- 34 torovich [1942] as a linear program (static formulation) enables the 35 use of convex analysis to study its structure and develop numerical 36 solvers. The equivalence between these two formulations was 37 introduced by Brenier [1991] and opened the door to a dynamical 38 (geodesic) reformulation [Benamou and Brenier 2000]. We refer 39 to [Santambrogio 2015] for a review of the theoretical foundations 40 of OT.

The basic OT problem has been extended in various ways, a typical 42 illustration of which being the computation of a barycenter (Fréchet 43 mean) of input measures, a convex program studied by Aguech and 44 Carlier [2011]. OT has found numerous applications, for instance in 45 computer vision (under the name “earth mover distance”) [Rubner 46 et al. 2000] or computer graphics [Bonneel et al. 2011].

**48 Unbalanced transport.** While the initial formulations of OT are 49 restricted to positive measures of equal mass (normalized probability 50 distributions), a recent wave of activity has proposed and studied 51 a family of “canonical” extensions to the “unbalanced” setting of 52 arbitrary positive measures. This covers both a dynamic formulation 53 [Liero et al. 2016; Kondratyev et al. 2015; Chizat et al. 2016b] 54 and a static one [Liero et al. 2015; Chizat et al. 2015] and has been 55 applied in machine learning [Frogner et al. 2015]. Our work extends 56 this static unbalanced formulation to tensor-valued measures.

**57 Entropic regularization.** The current state-of-the-art OT approx- 58 imation for arbitrary ground costs uses entropic regularization of 59 the transport plan. This leads to strictly convex programs that can 60 be solved using a simple class of highly parallelizable “diagonal 61 scaling” algorithms. The landmark paper of Cuturi [2013] inspired 62 detailed study of these solvers, leading to various generalizations 63 of Sinkhorn’s algorithm [1964]. This includes for instance the use

fast convolutional structures [Solomon et al. 2015], extensions to barycenters [Benamou et al. 2015] and to unbalanced OT [Frogner et al. 2015; Chizat et al. 2016a]. These entropic regularization techniques correspond to the use of projection and proximal maps for the Kullback–Leibler Bregman divergence and are equivalent to iterative projections [Bregman 1967] and Dykstra’s algorithm [Dykstra 1983; Bauschke and Lewis 2000]. An important contribution of the present work is to extend these techniques to the matrix setting (i.e., using quantum divergences). Note that quantum divergences have been recently used to solve some machine learning problems [Dhillon and Tropp 2008; Kulis et al. 2009; Chandrasekaran and Shah 2016].

**Tensor field processing.** Tensor-valued data are ubiquitous in various areas of imaging science, computer graphics and vision. In medical imaging, diffusion tensor imaging (DTI) [Wandell 2016] directly maps observed data to fields of tensors, and specific processing methods have been developed (see e.g. [Dryden et al. 2009; Deriche et al. 2006]). Tensor fields are also at the heart of anisotropic diffusions techniques in image processing [Weickert 1998], anisotropic meshing [Alliez et al. 2003; Demaret et al. 2006; Bougleux et al. 2009], anisotropic texture generation [Lagae et al. 2011], and find applications to line drawing [Vaxman et al. 2016] and data visualization [Hotz et al. 2004].

**OT on tensor fields.** The simplest way to define OT-like distances between arbitrary vector-valued measures is to use dual norms [Ning and Georgiou 2014], which correspond to generalizations of  $W_1$  OT for which transport cost equals ground distance. The corresponding metrics, however, have degenerate behavior in interpolation and barycenter problems (much like the  $L^1$  norm on functions) and only use the linear structure of matrices rather than their multiplicative structure. More satisfying notions of OT have recently been proposed in a dynamical (geodesic) way [Jiang et al. 2012; Carlen and Maas 2014; Chen et al. 2016]. A static formulation of a tensor-valued OT is proposed in [Ning et al. 2015], but it differs significantly from ours. It is initially motivated using a lifting that squares the number of variables, but a particular choice of cost reduces the computation to the optimization of a pair of couplings. In contrast, the formulation we propose in the present article is a direct generalization of unbalanced OT to matrices, which in turn enables the use of a Sinkhorn algorithm.

## 1.2 Contributions

We present a new static formulation of OT between tensor fields, which is the direct generalization of unbalanced OT from the scalar to the matrix case. Our second contribution is a fast entropic scaling algorithm generalizing the celebrated Sinkhorn iterative scheme. This leads to a method to compute geometrically-faithful interpolations between two tensor fields. Our third contribution is the extension of this approach to compute barycenters between several tensor fields. The Matlab code to reproduce the results of this article is available online.<sup>1</sup>

## 1.3 Notation

In the following, we denote  $\mathcal{S}^d \subset \mathbb{R}^{d \times d}$  the space of symmetric matrices,  $\mathcal{S}_+^d$  the closed convex cone of positive semidefinite matrices, and  $\mathcal{S}_{++}^d$  the open cone of positive definite matrices. We denote  $\exp : \mathcal{S}^d \rightarrow \mathcal{S}_{++}^d$  the matrix exponential, which is defined as  $\exp(P) = U \text{diag}_s(e^{\sigma_s})U^\top$  where  $P = U \text{diag}_s(\sigma_s)U^\top$  is an eigendecomposition of  $P$ . We denote  $\log : \mathcal{S}_{++}^d \rightarrow \mathcal{S}^d$  the matrix

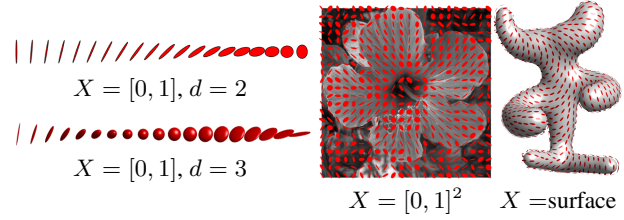


**Figure 2:** Displays of various types of tensor-valued measures  $\mu$ . The principal directions of an ellipse at some  $x_i \in X$  are the eigenvectors of  $\mu_i \in \mathcal{S}_+^d$ , while the principal width are given by its eigenvalues.

logarithm  $\log(P) = U \text{diag}_s(\log \sigma_s)U^\top$ , which is the inverse of  $\exp$  on  $\mathcal{S}_{++}^d$ .

A tensor-valued measure  $\mu$  defined on some space  $X$  is a vector-valued measure, where the “mass”  $\mu(A) \in \mathcal{S}_+^d$  associated to a measurable set  $A \subset X$  is a PSD matrix. In this article, in order to derive computational schemes, we focus on discrete measures. Such a measure  $\mu$  is a sum of Dirac masses  $\mu = \sum_{i \in I} \mu_i \delta_{x_i}$  where  $(x_i)_i \subset X$ , and  $(\mu_i)_i \in \mathcal{S}_+^d$  is a collection of PSD matrices. In this case,  $\mu(A) = \sum_{x_i \in A} \mu_i$ . Figure 2 shows graphically some examples of tensor-valued measures; we use this type of visualization through the article. In the following, since the sampling points  $(x_i)_i$  are assumed to be fixed and clear from the context, to ease readability, we do not make the distinction between the measure  $\mu$  and the collection of matrices  $(\mu_i)_i$ . This is an abuse of notation, but it is always clear from context whether we are referring to a measure or a collection of matrices.

The quantum entropy (also called von Neumann entropy) of a tensor-valued measure is

$$H(\mu) \stackrel{\text{def.}}{=} \sum_i H(\mu_i) \quad \text{where} \quad (1)$$

$$\forall P \in \mathcal{S}^d, \quad H(P) \stackrel{\text{def.}}{=} -\text{tr}(P \log(P) - P) - \iota_{\mathcal{S}_+^d}(P),$$

where  $\iota_C$  is the indicator function of a closed convex set  $C$ , i.e.  $\iota_C(P) = 0$  if  $P \in C$  and  $\iota_C(P) = +\infty$  otherwise. Note that  $H$  is a concave function. The quantum Kullback-Leibler divergence (also called quantum relative entropy) is the Bregman divergence associated to  $-H$ . For a collection of PSD matrices  $\mu = (\mu_i)_i, \xi = (\xi_i)_i$  in  $\mathcal{S}_+^d$  corresponding to measures defined on the same grid, assuming  $\xi_i \in \mathcal{S}_{++}^d$ , it is defined as

$$\text{KL}(\mu|\xi) \stackrel{\text{def.}}{=} \sum_i \text{KL}(\mu_i|\xi_i), \quad (2)$$

where for all  $(P, Q) \in \mathcal{S}_+^d \times \mathcal{S}_{++}^d$ , we denote

$$\text{KL}(P|Q) \stackrel{\text{def.}}{=} \text{tr}(P(\log(P) - \log(Q)) - P + Q) + \iota_{\mathcal{S}_{++}^d}(P)$$

which is convex with respect to both arguments. The inner product between collections of matrices  $\mu = (\mu_i)_i, \xi = (\xi_i)_i$  is

$$\langle \mu, \xi \rangle \stackrel{\text{def.}}{=} \sum_i \langle \mu_i, \xi_i \rangle \stackrel{\text{def.}}{=} \sum_i \text{tr}(\mu_i \xi_i^\top).$$

Given a collection of matrices  $\gamma = (\gamma_{i,j})_{i \in I, j \in J}$  the marginalization operators read

$$\gamma \mathbb{1}_J \stackrel{\text{def.}}{=} \left( \sum_j \gamma_{i,j} \right)_i \quad \text{and} \quad \gamma^\top \mathbb{1}_I \stackrel{\text{def.}}{=} \left( \sum_i \gamma_{i,j} \right)_j.$$

<sup>1</sup>Available as supplementary material.

## 2 Kantorovich Problem for Tensor-Valued Transport

We consider two measures that are sums of Dirac masses

$$\mu = \sum_{i \in I} \mu_i \delta_{x_i} \quad \text{and} \quad \nu = \sum_{j \in J} \nu_j \delta_{y_j} \quad (3)$$

where  $(x_i)_i \subset X$  and  $(y_j)_j \subset Y$ , and  $(\mu_i)_i \in \mathcal{S}_+^d$  and  $(\nu_j)_j \in \mathcal{S}_+^d$  are collections of PSD matrices. Our goal is to propose a new definition of OT between  $\mu$  and  $\nu$ .

### 2.1 Tensor Transportation

Following the initial static formulation of OT by Kantorovich [1942], we define a coupling  $\gamma = \sum_{i,j} \gamma_{i,j} \delta_{(x_i, y_j)}$  as a measure over the product  $X \times Y$  that encodes the transport of mass between  $\mu$  and  $\nu$ . In the matrix case,  $\gamma_{i,j} \in \mathcal{S}_+^d$  is now a PSD matrix, describing how much of mass is moved between  $\mu_i$  and  $\nu_j$ . Exact (balanced) transport would mean that the marginals  $(\gamma \mathbb{1}_J, \gamma^\top \mathbb{1}_I)$  must be equal to the input measures  $(\mu, \nu)$ . But as remarked by Ning et al. [2015], in contrast to the scalar case, in the matrix case (dimension  $d > 1$ ), this constraint is in general too strong, and there might exists no coupling satisfying these marginal constraints. We advocate in this work that the natural workaround for the matrix setting is the unbalanced case, and following [Liero et al. 2015], we propose to use a “relaxed” formulation where the discrepancy between the marginals  $(\gamma \mathbb{1}_J, \gamma^\top \mathbb{1}_I)$  and the input measures  $(\mu, \nu)$  is quantified according to some divergence between measures.

In the scalar case, the most natural divergence is the Kulback-Leibler divergence (which in particular gives rise to a natural Riemannian structure on positive measures, as defined in [Liero et al. 2016; Kondratyev et al. 2015; Chizat et al. 2016b]). We propose to make use of its quantum counterpart (2) via the following convex program

$$W(\mu, \nu) = \min_{\gamma} \langle \gamma, c \rangle + \rho_1 \text{KL}(\gamma \mathbb{1}_J | \mu) + \rho_2 \text{KL}(\gamma^\top \mathbb{1}_I | \nu) \quad (4)$$

subject to the constraint  $\forall (i, j), \gamma_{i,j} \in \mathcal{S}_+^d$ . Here  $\rho_1, \rho_2 > 0$  are constants balancing the “transport” effect versus the local modification of the matrices.

The matrix  $c_{i,j} \in \mathbb{R}^{d \times d}$  measures the cost of displacing an amount of (matrix) mass  $\gamma_{i,j}$  between  $x_i$  and  $y_j$  as  $\text{tr}(\gamma_{i,j} c_{i,j})$ . A typical cost, assuming  $X = Y$  is a metric space endowed with a distance  $d_X$ , is

$$c_{i,j} = d_X(x_i, y_j)^\alpha \text{Id}_{d \times d},$$

for some  $\alpha > 0$ . In this case, one should interpret the trace as the global mass of a tensor, and the total transportation cost is simply

$$\langle \gamma, c \rangle = \sum_{i,j} d_X(x_i, y_j)^\alpha \text{tr}(\gamma_{i,j}).$$

**Remark 1** (Classical OT). In the scalar case  $d = 1$ , (4) recovers exactly the log-entropic definition [Liero et al. 2015] of unbalanced optimal transport, which is studied numerically by Chizat et al. [2016a]. For isotropic tensors, i.e., all  $\mu_i$  and  $\nu_j$  are scalar multiples of the identity  $\text{Id}_{d \times d}$ , the computation also collapses to the scalar case (the  $\gamma_{i,j}$  are also isotropic). More generally, if all the  $(\mu_i, \nu_j)_{i,j}$  commute, they diagonalize in the same orthogonal basis, and (4) reduces to performing  $d$  independent unbalanced OT computations along each eigendirection.

**Remark 2** (Cost between single Dirac masses). When  $\mu = P \delta_x$  and  $\nu = Q \delta_x$  are two Dirac masses are the same location  $x$  and

associated to tensors  $(P, Q) \in (\mathcal{S}_+^d)^2$ , one obtains the following “metric” between tensors (assuming  $\rho_1 = \rho_2 = \rho$  for simplicity)

$$W(P \delta_x, Q \delta_x) = D(P, Q) \stackrel{\text{def.}}{=} \text{tr}(P + Q - 2\mathfrak{M}(P, Q))^{\frac{1}{2}} \quad (5)$$

where  $\mathfrak{M}(P, Q) \stackrel{\text{def.}}{=} \exp(\log(P)/2 + \log(Q)/2)$ . Unfortunately, in general  $D$  does not satisfy the triangle inequality. Note that when  $(P, Q)$  commute, one has  $D(P, Q) = \|\sqrt{P} - \sqrt{Q}\|$  which indeed satisfies the triangle inequality.

**Remark 3** (Quantum transport on curved geometries). If  $(\mu, \nu)$  are defined on a non-Euclidean space  $Y = X$ , like a smooth manifold, then formulation (4) should be handled with care, since it assumes all the tensors  $(\mu_i, \nu_j)_{i,j}$  are defined in some common basis. For smooth manifolds, the simplest workaround is to assume that these tensors are defined with respect to carefully selected orthogonal bases of the tangent planes, so that the field of bases is itself smooth. Unless the manifold is parallelizable, in particular if it has a trivial topology, it is not possible to obtain a globally smooth orthonormal basis; in general, any such field necessarily has a few singular points. In the following, we compute smoothly-varying orthogonal bases of the tangent planes following the method of Crane et al. [2010]. In this setting, the cost is usually chosen to be  $c_{i,j} = d_X(x_i, x_j)^\alpha \text{Id}_{d \times d}$  where  $d_X$  is the geodesic distance on  $X$ .

### 2.2 Quantum Transport Interpolation

Given two input measures  $(\mu, \nu)$ , we denote  $\gamma$  as a solution of (4) or, in practice, its regularized version (see (7) below). The coupling  $\gamma$  defines a (fuzzy) correspondence between the tensor fields. A typical use of this correspondence is to compute a continuous interpolation between these fields. Section 3.3 shows some numerical illustrations of this interpolation. Note also that Section 4 proposes a generalization of this idea to compute an interpolation (barycenter) between more than two input fields.

Mimicking the definition of the optimal transport interpolation (the so-called McCann displacement interpolation; see for instance [Santambrogio 2015]), we propose to use  $\gamma$  to define a path  $t \in [0, 1] \mapsto \mu_t$  interpolating between  $(\mu, \nu)$ . For simplicity, we assume the cost has the form  $c_{i,j} = d_X(x_i, y_j)^\alpha \text{Id}_{d \times d}$  for some ground metric  $d_X$  on  $X = Y$ . We also suppose we can compute efficiently the interpolation between two points  $(x_i, y_j) \in X^2$  as

$$x_{i,j}^t \stackrel{\text{def.}}{=} \underset{x \in X}{\text{argmin}} (1-t)d_X^2(x_i, x) + td_X^2(y_j, x).$$

For instance, over Euclidean spaces,  $g_t$  is simply a linear interpolation, and over more general manifold, it is a geodesic segment. We also denote

$$\bar{\mu}_i \stackrel{\text{def.}}{=} \mu_i \left( \sum_j \gamma_{i,j} \right)^{-1} \quad \text{and} \quad \bar{\nu}_j \stackrel{\text{def.}}{=} \nu_j \left( \sum_i \gamma_{i,j} \right)^{-1}$$

the adjustment factors which account for the imperfect match of the marginal associated to a solution of (7); the adjusted coupling is

$$\gamma_{i,j}^t \stackrel{\text{def.}}{=} [(1-t)\bar{\mu}_i + t\bar{\nu}_j]\gamma_{i,j}.$$

Finally, the interpolating measure is then defined as

$$\forall t \in [0, 1], \quad \mu_t \stackrel{\text{def.}}{=} \sum_{i,j} \gamma_{i,j}^t \delta_{x_{i,j}^t}. \quad (6)$$

One easily verifies that this measure indeed interpolates the two input measures, i.e.  $(\mu_{t=0}, \mu_{t=1}) = (\mu, \nu)$ . This formula (6) generates the interpolation by creating a Dirac tensor  $\gamma_{i,j}^t \delta_{x_{i,j}^t}$  for each coupling entry  $\gamma_{i,j}$ , and this tensor travels between  $\mu_i \delta_{x_i}$  (at  $t = 0$ ) and  $\nu_j \delta_{y_j}$  (at  $t = 1$ ).



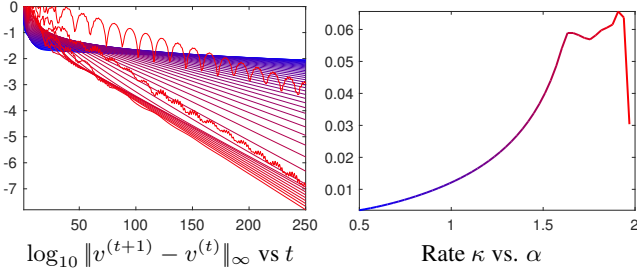


**Figure 3:** Display of convergence of Sinkhorn Algorithm 1 for the example displayed on the first row of Figure 1. Denoting  $u^{(t)}$  the value of the variable  $u$  at iteration  $t$ , the left plot shows the fixed point residual error for increasing values of  $\tau_1 = \tau_2 = \frac{\alpha\varepsilon}{\varepsilon+\rho}$  with  $\alpha \in [0.5, 2]$  (blue to red). The algorithm exhibits a linear convergence rate,  $\log_{10} \|v^{(t+1)} - v^{(t)}\|_\infty \sim -\kappa t$  for some  $\kappa > 0$ , and the right plot displays  $\kappa$  as a function of  $\alpha$ .

```

function QUANTUM-SINKHORN( $\mu, \nu, c, \varepsilon, \rho_1, \rho_2$ )
   $\forall k = 1, 2, \dots, \lceil \frac{2\varepsilon}{\varepsilon+\rho_k} \rceil$ ,
   $\forall (i, j) \in I \times J, (u_i, v_j) \leftarrow (0_{d \times d}, 0_{d \times d})$ 
  for  $s = 1, 2, 3, \dots$ 
     $K \leftarrow \mathcal{K}(u, v)$ 
     $\forall i \in I, u_i \leftarrow \text{LSE}_j(K_{i,j}) - \log(\mu_i)$ 
     $K \leftarrow \mathcal{K}(u, v)$ 
     $\forall j \in J, v_j \leftarrow \text{LSE}_i(K_{i,j}) - \log(\nu_j)$ 
  return  $(\gamma_{i,j} = \exp(K_{i,j}))_{i,j}$ 

```

**Algorithm 1:** Quantum-Sinkhorn iterations to compute the optimal coupling  $\gamma$  of the regularized transportation problem (7). The operator  $\mathcal{K}$  is defined in (9).

323 **Remark 7** (log and exp computations). A major computational work-  
 324 load of the Q-Sinkhorn Algorithm 1 is the repetitive computation of  
 325 matrix exp and log. For  $d \in \{2, 3\}$  it is possible to use closed form  
 326 expressions to diagonalize the tensors, so that the overall complexity  
 327 is comparable with the usual scalar case  $d = 1$ . While the applica-  
 328 tions Section 5 only considers these low-dimensional settings, high  
 329 dimensional problems are of interest, typically for machine learning  
 330 applications. In these cases, one has to resort to iterative procedures,  
 331 such as rapidly converging squaring schemes [Al-Mohy and Higham  
 332 2009; Al-Mohy and Higham 2012].

333 **Remark 8** (Computational complexity). For low-dimensional prob-  
 334 lems (typically for those considered in Section 5), the Q-Sinkhorn  
 335 Algorithm 1 scales to grid sizes of roughly 6k points (with machine-  
 336 precision solutions computed in a few minutes on a standard laptop).  
 337 For large scale grids, even storing the full coupling  $\gamma$  becomes pro-  
 338hibitive. We however observed numerically that, similarly to the  
 339 usual scalar case, the optimal  $\gamma$  solving (7) is highly sparse (up to  
 340 machine precision for small enough  $\varepsilon$ ). We thus found that using  
 341 the multi-scale refinement strategy introduced in [Schmitzer 2016]  
 342 is able to make the Q-Sinkhorn scales to high resolution grids. It is  
 343 not used to produce the figures of this article, but it is available in  
 344 the companion computational toolbox.

### 3.3 Numerical Illustrations

346 Figures 1 and 4 illustrates on synthetic examples of input tensor  
 347 fields  $(\mu, \nu)$  our interpolation method. We recall that it is obtained  
 348 in two steps:

- 349 1. One first computes the optimal  $\gamma$  solving (7) using Sinkhorn

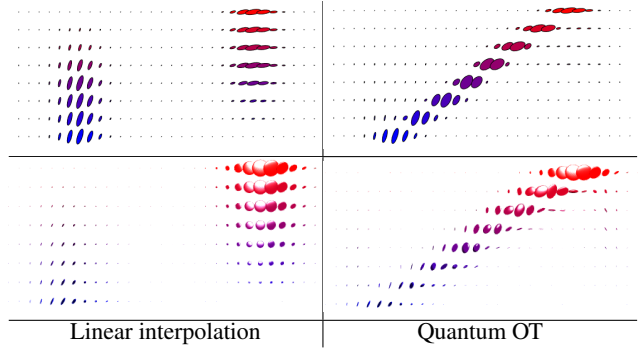


**Figure 4:** Comparison of linear and quantum-OT interpolation (using formula (6)). Each row shows a field of tensors (top  $d = 2$ , bottom  $d = 3$ ) along a linear segment from  $t = 0$  to  $t = 1$  ( $t$  axis is vertical).

350 iterations (Algorithm 1).

- 351 2. Then, for any  $t \in [0, 1]$ , one computes  $\mu_t$  using this optimal  $\gamma$   
 352 with formula (6).

353 Figure 4 shows examples of interpolations on a 1-D domain  $X =$   
 354  $Y = [0, 1]$  with tensors of dimension  $d = 2$  and  $d = 3$ , and a ground  
 355 cost  $c_{i,j} = |x_i - y_j|^2 \text{Id}_{d \times d}$ . It compares the OT interpolation, which  
 356 achieves a “mass displacement,” to the usual linear interpolation  
 357  $(1-t)\mu + t\nu$ , which only performs a pointwise interpolation of the  
 358 tensors.

359 Figure 1 shows larger scale examples. The first row corresponds to  
 360  $X = Y = [0, 1]^2$  and  $d = 2$ , with cost  $c_{i,j} = \|x_i - y_j\|^2 \text{Id}_{2 \times 2}$ ,  
 361 which is a typical setup for image processing. The second row  
 362 corresponds to  $X = Y$  being a triangulated mesh of a surface, and  
 363 the cost is proportional to the squared geodesic distance  $c_{i,j} =$   
 364  $d_X(x_i, y_j)^2 \text{Id}_{2 \times 2}$ .

## 4 Quantum Barycenters

366 Following Aguech and Carlier [2011] (see also [Benamou et al. 2015;  
 367 Solomon et al. 2015] for numerical methods using entropic regular-  
 368 ization), we now propose a generalization of the OT problem (4),  
 369 where, instead of coupling only two input measures, one tries to  
 370 couple an arbitrary set of inputs, and compute their Fréchet means.

### 4.1 Barycenter Optimization Problem

372 Given some input measures  $(\mu^\ell)_\ell$ , the quantum barycenter problem  
 373 reads

$$\min_{\nu} \sum_{\ell} w_{\ell} W_{\varepsilon}(\mu^{\ell}, \nu), \quad (15)$$

374 where  $(w_{\ell})_{\ell}$  is a set of positive weights normalized so that  $\sum_{\ell} w_{\ell} =$   
 375 1. In the following, for simplicity, we set

$$\rho_1 = \rho \quad \text{and} \quad \rho_2 = +\infty$$

376 in the definition (4) of  $W_{\varepsilon}$ . Note that the choice  $\rho_2 = +\infty$  corre-  
 377 sponds to imposing the exact hard marginal constraint  $\gamma^{\top} \mathbb{1}_J = \nu$ .  
 378 **Remark 9** (Barycenters between single Dirac masses). If all the  
 379 input measures are concentrated on single Diracs  $\mu^{\ell} = P_{\ell} \delta_{x_{\ell}}$ , then  
 380 the single Dirac barycenter (unregularized, i.e.,  $\varepsilon = 0$ ) for a cost  
 381  $d_X(x, y)^{\alpha} \text{Id}_{d \times d}$  is  $P \delta_x^*$  where  $x^* \in X$  is the usual barycenter for  
 382 the distance  $d_X$ , solving

$$x^* \in \operatorname{argmin}_x \mathcal{E}(x) = \sum_{\ell} w_{\ell} d_X^{\alpha}(x_{\ell}, x)$$

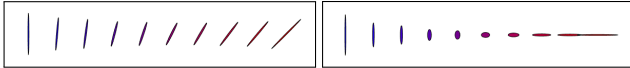


**Figure 5:** Two examples of pointwise (without transportation) interpolations (16). Here  $P_1$  and  $P_2$  are represented using the blue/red ellipses on the left/right, and weights are  $(w_1, w_2) = (1-t, t)$  for  $t \in [0, 1]$  from left to right.

```

function QUANTUM-BARYCENTER( $(\mu_\ell)_{\ell=1}^L, c, \varepsilon, \rho$ )
    Choose  $\tau_1 \in ]0, \frac{2\varepsilon}{\varepsilon+\rho}[$ ,  $\tau_2 \in ]0, 2[$ .
     $\forall (i, j) \in I \times J, (u_i, v_j) \leftarrow (0_{d \times d}, 0_{d \times d})$ 
    for  $s = 1, 2, 3, \dots$ 
        for  $\ell = 1, \dots, L$ 
             $K^\ell \leftarrow \mathcal{K}(u^\ell, v^\ell),$ 
             $\forall i \in I, u_i^\ell \xleftarrow{\tau_1} \text{LSE}_j(K_{i,j}^\ell) - \log(\mu_i^\ell),$ 
             $K^\ell \leftarrow \mathcal{K}(u^\ell, v^\ell).$ 
         $\forall j \in J, \log(\nu_j) \leftarrow \sum_\ell w_\ell (\text{LSE}_i(K_{i,j}^\ell) + v_j^\ell / \varepsilon).$ 
        for  $\ell = 1, \dots, L$ 
             $\forall j \in J, v_j^\ell \xleftarrow{\tau_2} \varepsilon \text{LSE}_i(K_{i,j}^\ell) + v_j^\ell - \varepsilon \log(\nu_j).$ 
    return  $\nu$ 

```

**Algorithm 2:** Quantum-Barycenter iterations to compute the optimal barycenter measure  $\nu$  solving (15). The operator  $\mathcal{K}$  is defined in (18).

and the barycentric matrix is

$$P = e^{-\frac{\varepsilon(x^*)}{\rho}} \exp \left( \sum_\ell w_\ell \log(P_\ell) \right). \quad (16)$$

Figure 5 illustrates the effect of a pointwise interpolation (i.e. at the same location  $x_\ell$  for all  $\ell$ ) between tensors.

Problem (15) is convex, and similarly to (8), it can be rewritten in dual form.

**Proposition 3.** The optimal  $\nu$  solving (15) is solution of

$$\max_{(u^\ell, v^\ell)} \min_{\nu} - \sum_\ell w_\ell \text{tr} \left[ \rho \sum_i e^{u_i^\ell + \log(\mu_i^\ell)} + \sum_j \nu_j v_j^\ell + \varepsilon \sum_{i,j} e^{\mathcal{K}(u^\ell, v^\ell)_{i,j}} \right], \quad (17)$$

where here we define  $\mathcal{K}$  as

$$\mathcal{K}(u, v)_{i,j} \stackrel{\text{def.}}{=} -\frac{c_{i,j} + \rho u_i + v_j}{\varepsilon}. \quad (18)$$

## 4.2 Quantum Barycenter Sinkhorn

Similarly to Proposition 2, the dual solutions of (17) satisfy a set of coupled fixed point equations:

**Proposition 4.** Optimal  $(u^\ell, v^\ell)_{\ell}$  for (17) satisfy

$$\forall (i, \ell), \text{LSE}_j(\mathcal{K}(u^\ell, v^\ell)_{i,j}) - \log(\mu_i^\ell) = u_i^\ell \quad (19)$$

$$\forall (j, \ell), \text{LSE}_i(\mathcal{K}(u^\ell, v^\ell)_{i,j}) = \log(\nu_j) \quad (20)$$

$$\sum_\ell w_\ell v^\ell = 0. \quad (21)$$

*Proof.* The proof of (19) and (20) is the same as the one of Proposition 2. Minimization of (17) on  $\nu$  leads to (21).  $\square$

The extension of the quantum Sinkhorn algorithm to solve the barycenter problem (2) is detailed in Algorithm 2. It alternates between the updates of  $u$ ,  $\nu$  and  $v$ , using the relaxed version of the fixed point equations (19), (20) and (21). The notation  $\xleftarrow{\tau}$  refers to a relaxed assignment as defined in (14).

**Remark 10** (Choice of  $\tau$ ). Remark 5 also applies for this Sinkhorn-like scheme, and setting  $(\tau_1, \tau_2) = (\frac{\varepsilon}{\rho+\varepsilon}, 1)$  leads, in the scalar case  $d = 1$ , to the algorithm in [Chizat et al. 2016a]. We found experimentally that this choice leads to contracting (and hence linearly converging) iterations, and that higher values of  $\tau$  usually accelerate the convergence rate.

**Remark 11** (Scalar and isotropic cases). Note that in the scalar case  $d = 1$  and for isotropic input tensors (multiples of the identity), one retrieves the provably convergent unbalanced barycenter algorithm in [Chizat et al. 2016a].

## 4.3 Numerical Illustrations

Figure 6 shows examples of barycenters  $\nu$  solving (15) between four input measures  $(\mu^\ell)_{\ell=1}^4$ . The horizontal/vertical axes of the figures are indexed by  $(t_1, t_2) \in [0, 1]^2$  (on a  $5 \times 5$  grids) and parameterize the weights  $(w_\ell)_{\ell=1}^4$  appearing in (15) as

$$(w_1, w_2, w_3, w_4) \stackrel{\text{def.}}{=} ((1-t_1)(1-t_2), (1-t_1)t_2, t_1(1-t_2), t_1, t_2). \quad (22)$$

The left part of Figure 6 corresponds to measures on  $X = Y = [0, 1]^2$  with  $d = 2$  and ground cost  $c_{i,j} = \|x_i - x_j\|^2 \text{Id}_{2 \times 2}$ . The right part of Figure 6 corresponds to measures on  $X = Y$  being a surface mesh with  $d = 2$  (the tensors are defined on the tangent planes) and a ground cost is  $c_{i,j} = d_X(x_i, x_j)^2 \text{Id}_{2 \times 2}$  where  $d_X$  is the geodesic distance on the mesh.

## 5 Applications

This section showcases four different applications of Q-OT to register and interpolate tensor fields. Unless otherwise stated, the data is normalized to the unit cube  $[0, 1]^d$  (here  $d = 2$  for images) and discretized on grids of  $|I| = |J| = 60^d$  points. The regularization parameter is set to  $\varepsilon = 0.08^2$ , the fidelity penalty to  $\rho = 1$ , and the relaxation parameter for Sinkhorn to  $\tau_k = \frac{1.8\varepsilon}{\varepsilon + \rho_k}$ .

### 5.1 Anisotropic Space-Varying Procedural Noise

Texture synthesis using procedural noise functions is widely used in rendering pipelines and video games because of both its low storage cost and the fact that it is typically parameterized by a few meaningful parameters [Lagae et al. 2010]. Following Lagae et al. [2011] we consider here a spatially-varying Gabor noise function (i.e. non-stationary Gaussian noise), whose covariance function is parameterized using a PSD-valued field  $\mu$ . Quantum optimal transport allows to interpolate and navigate between these noise functions by transporting the corresponding tensor fields. The initial Gabor noise method makes use of sparse Gabor splattering [Lagae et al. 2010] (which enables synthesis at arbitrary resolution and zooming). For simplicity, we rather consider here a more straightforward method, where the texture  $f_{t_0}$  is obtained by stopping at time  $t = t_0$  an anisotropic diffusion guided by the tensor field  $\mu$  of a high frequency noise  $\mathcal{N}$  (numerically a white noise on a grid)

$$\frac{\partial_t f_t}{\partial t} = \text{div}(\mu \nabla f_t), \quad \text{where } f_{t=0} \sim \mathcal{N},$$

where  $(\mu \nabla f_t)(x) \stackrel{\text{def.}}{=} \mu(x)(\nabla f_t(x))$  is the vector field obtained by applying the tensor  $\mu(x) \in \mathcal{S}_2^+$  to the gradient vector  $\nabla f_t(x) \in \mathbb{R}^2$ . Locally around  $x$ , the texture is stretched in the direction of the

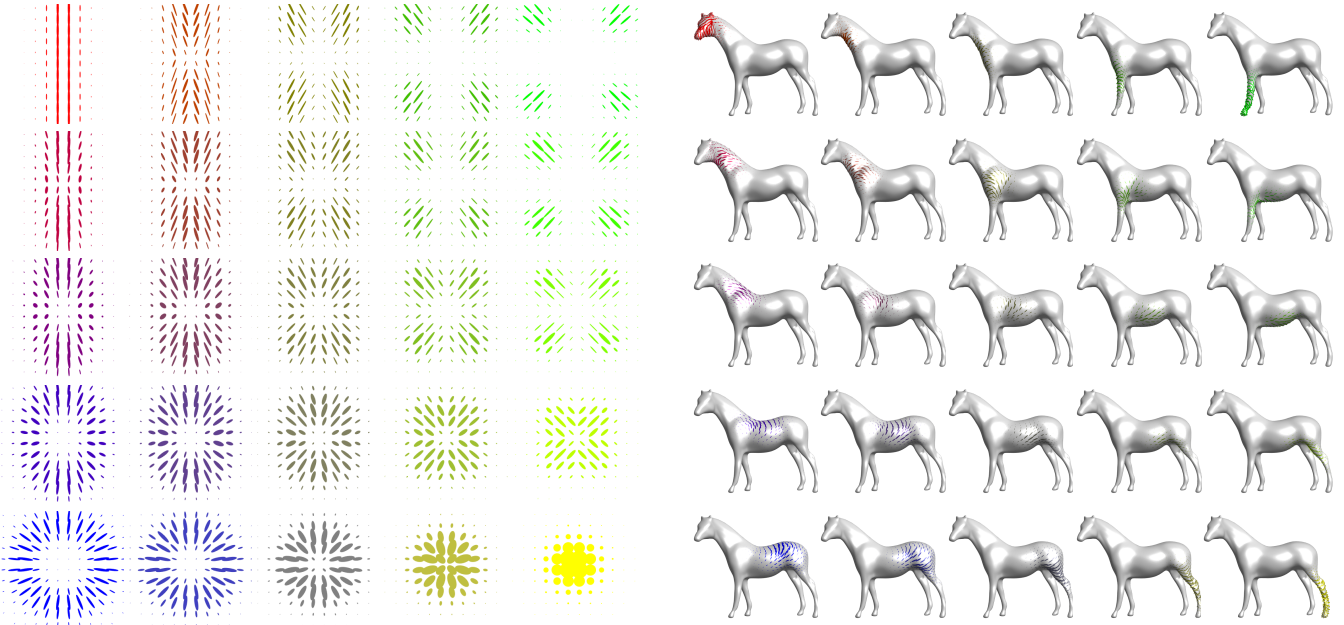


**Figure 6:**  $5 \times 5$  barycenters of four input measures (displayed in the four corners). The weights  $w \in \mathbb{R}^4$  correspond to bilinear interpolation weights (22) inside the square.

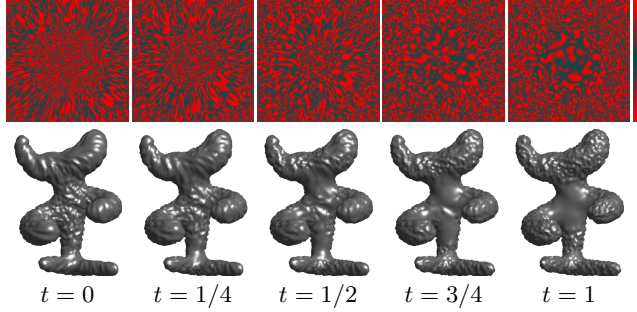


**Figure 7:** Example of interpolation between two input procedural anisotropic noise function. The PSD tensor field parameterizing the texture are displayed on Figure 1. The colormap used to render the anisotropic texture is displayed on the last column.

448 main eigenvector of  $\mu(x)$ , highly anisotropic tensor giving rise to  
449 elongated “stripes” as opposed to isotropic tensor generating “spots.”

450 Numerically,  $f$  is discretized on a 2-D grid, and  $\mu$  is represented on  
451 this grid as a sum of Dirac masses (3). On Euclidian domains  $X$ ,  $\nabla$   
452 and  $\text{div}$  are computed using finite differences, while on triangulated  
453 mesh, they are implemented using standard piecewise-linear finite  
454 element primitives. Figure 7 shows two illustrations of this method.  
455 The top row generates an animated color texture by indexing a non-  
456 linear black-red colormap (displayed on the right) using  $f_t$ . Bottom  
457 row generates an animated bump-mapped surface using  $f_t$  to offset  
458 the mesh surface in the normal direction.

## 459 5.2 Anisotropic Meshing

460 Approximation with anisotropic piecewise linear finite elements  
461 on a triangulated mesh is a fundamental tool to address tasks such  
462 as discretizing partial differential equations, performing surface  
463 remeshing [Alliez et al. 2003] and image compression [Demaret

464 et al. 2006]. A common practice is to generate triangulations  
465 complying with a PSD tensor sizing field  $\mu$ , i.e. such that a tri-  
466 angle centered at  $x \in X$  should be inscribed in the ellipsoid  
467  $\{u \in X ; (u - x)^\top \mu(x)(u - x) \leq \delta\}$  for some  $\delta$  controlling the  
468 triangulation density. A well-known result is that, to locally approx-  
469 imate a smooth convex  $C^2$  function  $f$ , the optimal shapes of triangles  
470 is dictated by the Hessian  $Hf$  of the function (see [Shewchuk 2002]).  
471 In practice, people use  $\mu(x) = |Hf(x)|^\alpha$  for some exponent  $\alpha > 0$   
472 (which is related to the quality measure of the approximation), where  
473  $|\cdot|^\alpha$  indicates the spectral application of the exponentiation (as for  
474 matrix exp or log).

475 Figure (8) shows that Q-OT can be used (using formula (6)) to inter-  
476 polate between two sizing fields  $(\mu, \nu)$ , which are computed from the  
477 Hessians (with here  $\alpha = 1$ ) of two initial input images  $(f, g)$ . The  
478 resulting anisotropic triangulations are defined as geodesic Delau-  
479 nay triangulations for the Riemannian metric defined by the tensor  
480 field, and are computed using the method detailed in [Bougleux  
481 et al. 2009]. This interpolation could typically be used to track the  
482 evolution of the solution of some PDE.

## 483 5.3 Diffusion Tensor Imaging

484 Diffusion tensor magnetic resonance imaging (DTI) is a popular  
485 technique to image the white matter of the brain (see [Wandell  
486 2016] for a recent overview). DTI measures the diffusion of water  
487 molecules, which can be compactly encoded using a PSD tensor  
488 field  $\mu(x) \in \mathcal{S}_+^3$ , whose anisotropy and size matches the local  
489 diffusivity. A typical goal of this imaging technique is to map  
490 the brain anatomical connectivity, and in particular track the white  
491 matter fibers. This requires a careful handling of the tensor’s energy  
492 (its trace) and anisotropy, so that using Q-OT is a perfect fit for such  
493 data.

494 Figure 9 shows an application of Q-OT for the interpolation (using 6)  
495 between 2-D slices from DTI tensor fields  $(\mu, \nu)$  acquired on two  
496 different subjects. This data is extracted from the studies [Pestilli  
497 et al. 2014; Takemura et al. 2016]. These two patients exhibit differ-

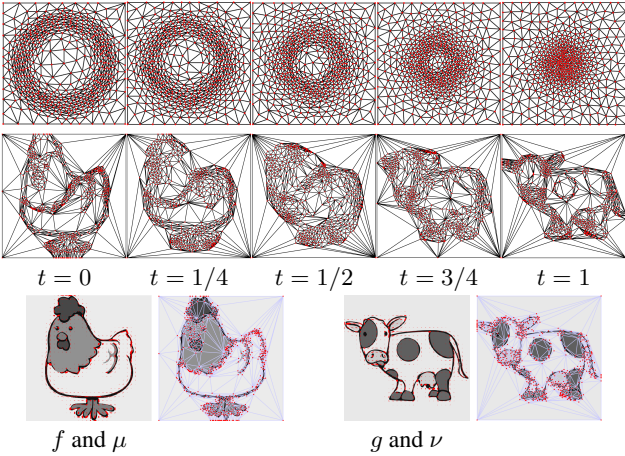


**Figure 8:** Two examples of interpolation between two input sizing fields  $(\mu_{t=0}, \mu_{t=1}) = (\mu, \nu)$ . **First row:** triangulation evolution for the sizing fields displayed on Figure 1. **Second row:** the input sizing fields  $(\mu_{t=0}, \mu_{t=1}) = (\mu, \nu)$  are displayed on the third row, and are defined using the absolute value ( $\alpha = 1$ ) of the Hessian of the underlying images ( $f, g$ ).

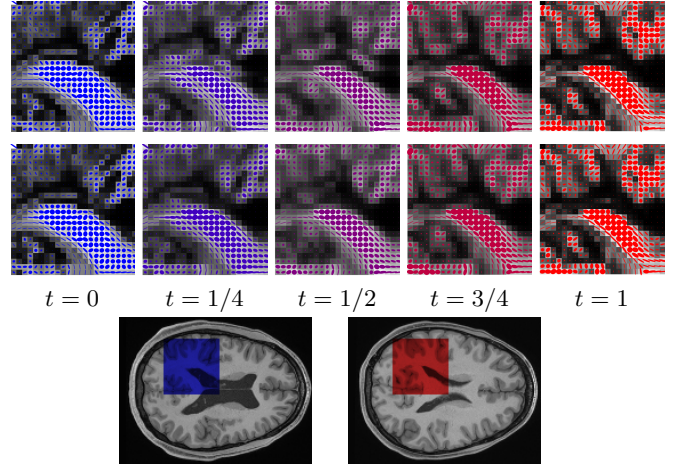


**Figure 9:** Interpolation between two 2-D slices of 3-D DTI tensor fields  $(\mu, \nu) = (\mu_{t=0}, \mu_{t=1})$ . For readability, only the X/Y components of the tensors are displayed. **First row:** interpolation obtained using  $\rho = 1$ . **Second row:** interpolation obtained using  $\rho = 0.5$ . **Third row:** anatomical MRI images indicating the region of interest where the computations are performed.

ent anatomical connectivity geometries, and Q-OT is able to track the variation in both orientation and magnitude of the diffusion tensors. This figure also compares the different data fidelity parameters  $\tau \in \{0.05, 1\}$ . Selecting  $\tau = 1$  enforces an overly-strong conservation constraint and leads to interpolation artifacts (in particular some structure are split during the interpolation). In contrast, selecting  $\tau = 0.05$  introduces enough mass creation/destruction during the interpolation to be able to cope with strong inter-subject variability.

498  
499  
500  
501  
502  
503  
504  
505  
531  
532  
533  
534  
535

a new texture  $F$  is synthesized and displayed. Note that while the Q-Sinkhorn Algorithm 1 is provided for real PSD matrices, it extends verbatim to complex positive hermitian matrices (the matrix logarithm and exponential being defined the same way as for real matrices).

## 6 Conclusion

In this work, we have proposed a new static formulation for OT between tensor-valued measures. This formulation is an extension of the recently proposed unbalanced formulation of OT. A chief advantage of this formulation is that, once coupled with quantum entropic regularization, it leads to an effective numerical scheme, which is easily extended to the computation of barycenters.

## Acknowledgements

DTI data were provided by Franco Pestilli (NSF IIS 1636893; NIH ULTR001108) and the Human Connectome Project (NIH 1U54MH091657). The images for the texture synthesis experiments are from IPOL<sup>2</sup>. The images for the triangular meshing experiments are from Wikimedia.

Initial results in this paper were shared in a non-peer-reviewed pre-publication [Anonymous 2016].

## References

- AGUEH, M., AND CARLIER, G. 2011. Barycenters in the Wasserstein space. *SIAM Journal on Mathematical Analysis* 43, 2, 904–924.
- AL-MOHY, A. H., AND HIGHAM, N. J. 2009. A new scaling and squaring algorithm for the matrix exponential. *SIAM J. Sci. Comput.* 31, 3, 970–989.

<sup>2</sup>[www.ipol.im](http://www.ipol.im)

516  
517  
518  
519  
520  
521  
522  
523  
524  
525  
526  
527  
536

ent anatomical connectivity geometries, and Q-OT is able to track the variation in both orientation and magnitude of the diffusion tensors. This figure also compares the different data fidelity parameters  $\tau \in \{0.05, 1\}$ . Selecting  $\tau = 1$  enforces an overly-strong conservation constraint and leads to interpolation artifacts (in particular some structure are split during the interpolation). In contrast, selecting  $\tau = 0.05$  introduces enough mass creation/destruction during the interpolation to be able to cope with strong inter-subject variability.

## 5.4 Spectral Color Texture Synthesis

As advocated initially in [Galerne et al. 2011], a specific class of textured images (so-called micro-textures) is well-modeled using stationary Gaussian fields. In the following, we denote  $p$  the pixel positions and  $x$  the Fourier frequency indices. For color images, these fields are fully characterized by their mean  $m \in \mathbb{R}^3$  and their Fourier power spectrum, which is a tensor valued field  $\mu(x)$  where, for each frequency  $x$  (defined on a 2-D grid)  $\mu(x) \in \mathbb{C}^{3 \times 3}$  is a complex positive semi-definite hermitian matrix. In practice,  $\mu(x)$  is estimated from an exemplar color image  $f(p) \in \mathbb{R}^3$  using an empirical spectrogram

$$\mu(x) \stackrel{\text{def}}{=} \frac{1}{K} \sum_{k=1}^K \hat{f}_k(x) \hat{f}_k(x)^* \in \mathbb{C}^{3 \times 3} \quad (23)$$

where  $\hat{f}_k$  is the Fourier transform of  $f_k(p) \stackrel{\text{def}}{=} f(p)w_k(p)$  (computed using the FFT),  $w_k$  are windowing functions centred around  $K$  locations in the image plane, and  $v^* \in \mathbb{C}^{1 \times 3}$  denoted the transpose-conjugate of a vector  $v \in \mathbb{C}^{3 \times 1}$ . Increasing the number  $K$  of windowed estimations helps to avoid having rank-deficient covariances ( $K = 1$  leads to a field  $\mu$  of rank-1 tensors). Randomized new textures are then created by generating random samples  $F(p) \in \mathbb{R}^3$  from the Gaussian field, which is achieved by defining the Fourier transform  $\hat{F}(x) \stackrel{\text{def}}{=} \hat{N}(x)\sqrt{\mu(x)}\mathbf{1}_3$ , where  $N(p)$  is the realization of a Gaussian white noise, and  $\sqrt{\cdot}$  is the matrix square root (see [Galerne et al. 2011] for more details).

Figure 10 shows an application where two input power spectra  $(\mu, \nu)$  (computed using (23) from two input textures exemplars  $(f, g)$ ) are interpolated using (6), and for each interpolation parameter  $t \in [0, 1]$

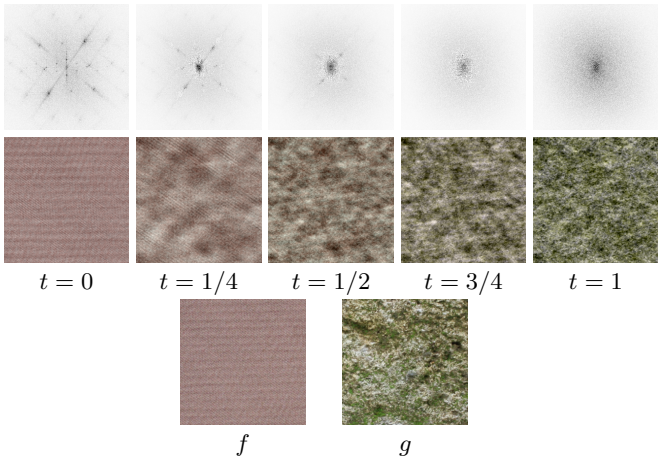


**Figure 10:** *First row:* display  $\text{tr}(\mu_t(x))$  where  $\mu_t$  are the interpolated power spectra. *Second row:* realizations of the Gaussian field parameterized by the power spectra  $\mu_t$ . *Third row:* input texture exemplars from which  $(\mu_{t=0}, \mu_{t=1}) = (\mu, \nu)$  are computed.

- 594 CHANDRASEKARAN, V., AND SHAH, P. 2016. Relative entropy  
595 optimization and its applications. *Mathematical Programming*,  
596 1–32.
- 597 CHEN, Y., GEORGIOU, T. T., , AND TANNENBAUM, A. 2016. Dis-  
598 tances and Riemannian metrics for multivariate spectral densities.  
599 *Preprint arXiv:1610.03041*.
- 600 CHIZAT, L., PEYRÉ, G., SCHMITZER, B., AND VIALARD, F.-X.  
601 2015. Unbalanced optimal transport: Geometry and Kantorovich  
602 formulation. *Preprint 1508.05216*, Arxiv.
- 603 CHIZAT, L., PEYRÉ, G., SCHMITZER, B., AND VIALARD, F.-X.  
604 2016. Scaling algorithms for unbalanced transport problems.  
605 *Preprint 1607.05816*, Arxiv.
- 606 CHIZAT, L., SCHMITZER, B., PEYRÉ, G., AND VIALARD, F.-  
607 X. 2016. An interpolating distance between optimal transport  
608 and Fisher–Rao. *to appear in Foundations of Computational  
609 Mathematics*.
- 610 CRANE, K., DESBRUN, M., AND SCHRÖDER, P. 2010. Trivial  
611 connections on discrete surfaces. In *Computer Graphics Forum*,  
612 vol. 29, Wiley Online Library, 1525–1533.
- 613 CUTURI, M. 2013. Sinkhorn distances: Lightspeed computation of  
614 optimal transportation. In *Proc. NIPS*, vol. 26. 2292–2300.
- 615 DEMARET, L., DYN, N., AND ISKE, A. 2006. Image compression  
616 by linear splines over adaptive triangulations. *Signal Processing*  
617 86, 7, 1604–1616.
- 618 DERICHE, R., TSCHUMPELÉ, D., LENGLER, C., AND ROUSSON,  
619 M. 2006. *Variational Approaches to the Estimation, Regular-  
620 ization and Segmentation of Diffusion Tensor Images*. Springer  
621 US, Boston, MA, 517–530.
- 622 DHILLON, I. S., AND TROPP, J. A. 2008. Matrix nearness problems  
623 with Bregman divergences. *SIAM Journal on Matrix Analysis  
624 and Applications* 29, 4, 1120–1146.
- 625 DRYDEN, I. L., KOLOYDENKO, A., AND ZHOU, D. 2009. Non-  
626 Euclidean statistics for covariance matrices, with applications  
627 to diffusion tensor imaging. *The Annals of Applied Statistics*,  
628 1102–1123.
- 629 DYKSTRA, R. L. 1983. An algorithm for restricted least squares  
630 regression. *J. Amer. Stat.* 78, 384, 839–842.
- 631 FROGNER, C., ZHANG, C., MOBAHI, H., ARAYA, M., AND POG-  
632 GIO, T. 2015. Learning with a Wasserstein loss. In *Advances in  
633 Neural Information Processing Systems*, vol. 28. 2044–2052.
- 634 GALERNE, B., GOUSSEAU, Y., AND MOREL, J.-M. 2011. Random  
635 phase textures: Theory and synthesis. *IEEE Transactions on  
636 image processing* 20, 1, 257–267.
- 637 HOTZ, I., FENG, L., HAGEN, H., HAMANN, B., JOY, K. I., AND  
638 JEREMIC, B. 2004. Physically based methods for tensor field  
639 visualization. IEEE Computer Society, 123–130.
- 640 JIANG, X., NING, L., AND GEORGIOU, T. T. 2012. Distances  
641 and Riemannian metrics for multivariate spectral densities. *IEEE  
642 Transactions on Automatic Control* 57, 7 (July), 1723–1735.
- 643 KANTOROVICH, L. 1942. On the transfer of masses (in Russian).  
644 *Doklady Akademii Nauk* 37, 2, 227–229.
- 645 KONDRATYEV, S., MONSANGEON, L., AND VOROTNIKOV, D.  
646 2015. A new optimal transport distance on the space of finite  
647 Radon measures. Tech. rep., Pre-print.

- 648 KULIS, B., SUSTIK, M. A., AND DHILLON, I. S. 2009. Low-rank 703  
649 kernel learning with Bregman matrix divergences. *J. Mach. Learn.* 704  
650 *Res.* 10 (June), 341–376.
- 651 LAGAE, A., LEFEBVRE, S., COOK, R., DEROSSE, T., DRETTAKIS, 705  
652 G., EBERT, D. S., LEWIS, J., PERLIN, K., AND ZWICKER,  
653 M. 2010. A survey of procedural noise functions. In *Computer  
654 Graphics Forum*, vol. 29, Wiley Online Library, 2579–2600.
- 655 LAGAE, A., LEFEBVRE, S., AND DUTRÉ, P. 2011. Improving 706  
656 Gabor noise. *IEEE Transactions on Visualization and Computer  
657 Graphics* 17, 8, 1096–1107.
- 658 LIERO, M., MIELKE, A., AND SAVARÉ, G. 2015. Optimal entropy- 707  
659 transport problems and a new Hellinger–Kantorovich distance  
660 between positive measures. *ArXiv e-prints*.
- 661 LIERO, M., MIELKE, A., AND SAVARÉ, G. 2016. Optimal transport 708  
662 in competition with reaction: The Hellinger–Kantorovich distance  
663 and geodesic curves. *SIAM Journal on Mathematical Analysis*  
664 48, 4, 2869–2911.
- 665 MONGE, G. 1781. Mémoire sur la théorie des déblais et des 709  
666 remblais. *Histoire de l'Académie Royale des Sciences*, 666–704.
- 667 NING, L., AND GEORGIOU, T. T. 2014. Metrics for matrix-valued 710  
668 measures via test functions. In *53rd IEEE Conference on Decision  
669 and Control*, IEEE, 2642–2647.
- 670 NING, L., GEORGIOU, T. T., AND TANNENBAUM, A. 2015. On 711  
671 matrix-valued Monge–Kantorovich optimal mass transport. *IEEE  
672 transactions on automatic control* 60, 2, 373–382.
- 673 PESTILLI, F., YEATMAN, J. D., ROKEM, A., KAY, K. N., AND 713  
674 WANDELL, B. A. 2014. Evaluation and statistical inference for  
675 human connectomes. *Nature methods* 11, 10, 1058–1063.
- 676 ROCKAFELLAR, R. T. 1970. *Convex analysis*. Princeton University 714  
677 Press.
- 678 RUBNER, Y., TOMASI, C., AND GUIBAS, L. J. 2000. The earth 715  
679 mover’s distance as a metric for image retrieval. *International  
680 Journal of Computer Vision* 40, 2 (Nov.), 99–121.
- 681 SANTAMBROGIO, F. 2015. Optimal transport for applied mathe- 716  
682 maticians. *Progress in Nonlinear Differential Equations and their  
683 applications* 87.
- 684 SCHMITZER, B. 2016. Stabilized sparse scaling algorithms for 717  
685 entropy regularized transport problems. *arXiv:1610.06519*.
- 686 SHEWCHUK, J. 2002. What is a good linear finite element? Interpo- 718  
687 lation, conditioning, anisotropy, and quality measures (preprint).  
688 *University of California at Berkeley* 73.
- 689 SINKHORN, R. 1964. A relationship between arbitrary positive 719  
690 matrices and doubly stochastic matrices. *Ann. Math. Statist.* 35,  
691 876–879.
- 692 SOLOMON, J., DE GOES, F., PEYRÉ, G., CUTURI, M., BUTSCHER, 720  
693 A., NGUYEN, A., DU, T., AND GUIBAS, L. 2015. Convolu-  
694 tional Wasserstein distances: Efficient optimal transportation on  
695 geometric domains. *TOG* 34, 4 (July), 66:1–66:11.
- 696 TAKEMURA, H., CAIAFA, C. F., WANDELL, B. A., AND PESTILLI, 721  
697 F. 2016. Ensemble tractography. *PLoS Comput Biol* 12, 2,  
698 e1004692.
- 699 VAXMAN, A., CAMPEN, M., DIAMANTI, O., PANIZZO, D.,  
700 BOMMES, D., HILDEBRANDT, K., AND BEN-CHEN, M. 2016.  
701 Directional field synthesis, design, and processing. *Comput.  
702 Graph. Forum* 35, 2, 545–572.
- 705 WANDELL, B. A. 2016. Clarifying human white matter. *Annual  
Review of Neuroscience*.
- 706 WEICKERT, J. 1998. *Anisotropic diffusion in image processing*,  
vol. 1. Teubner Stuttgart.